Chemical Science

ROYAL SOCIETY OF CHEMISTRY

EDGE ARTICLE

View Article Online
View Journal

Cite this: DOI: 10.1039/d6sc03610d

All publication charges for this article have been paid for by the Royal Society of Chemistry

A spatially confined "double-key lock" smart DNA hydrogel for dynamic detection of MicroRNA in cells

Liyun Shi,[ab] Dandan Liang,[b] Jingyu Kuang,[b] Yuting He,[b] Dongyang Wang,*[b] Jiayi Shan,[b] Ziyang Wang,[b] Wei Shen,[b] Hian Kee Lee *[abc] and Sheng Tang *[ab]

Smart DNA hydrogels have attracted extensive attention in bioanalysis and biomedicine due to their programmable sol–gel phase transition ability and specific recognition characteristics of biomolecules. Herein, we propose a spatially confined "double-key lock" smart DNA hydrogel with temperature and target as double keys, which was constructed using poly(*N*-isopropylacrylamide)–acrylamide (NIPAM–AM) hydrogel as the carrier and aggregation-induced emission (AIE) type 1,1,2,2-tetra(4-carboxybenzene) ethylene (TCPE) as the fluorescence (FL) probe. This hydrogel exhibited a synergistic multi-response mechanism that combined the thermal phase transition of NIPAM–AM hydrogel, and the target recognition effect of complementary DNA strands. Upon concurrent stimulation by temperature elevation and target cDNA binding, this hydrogel underwent enhanced crosslinking, forming a denser three-dimensional network that restricted TCPE mobility and amplified its FL through aggregation. Molecular dynamics simulations further confirmed that the response mechanism involved the synergistic effect of thermodynamic equilibrium regulation and molecular configuration rearrangement. The combination of the smart DNA hydrogel and the rolling circle amplification (RCA) strategy realized the FL nucleic acid analysis of microRNA-21 (miRNA-21) as an analyte, exhibiting a wide linear response in the range of 0.1 fM to 10 nM with a limit of detection of 33.3 aM. Moreover, this platform was successfully applied to the quantitative analysis of miRNA-21 in the serum of lung cancer and gastric cancer patients, and can *in situ* track the secretion behavior of tumor cell derived miRNA-21. This strategy provides new insights into the multi-scale design of temperature–biomolecular double-responsive smart nanomaterials and offers a promising strategy for advanced biosensing and bioanalytical applications.

Received 29th April 2026
Accepted 1st June 2026

DOI: 10.1039/d6sc03610d

rsc.li/chemical-science

Introduction

Stimulation-responsive hydrogels have emerged as a major research focus owing to their ability to convert environmental cues into structural or functional changes, offering broad prospects for biomedical and analytical applications.[1,2] To further enhance the specific recognition ability and selective response performance of this kind of stimulation-responsive hydrogel, biological molecules (such as DNA) were introduced and functionalized to build a multifunctional integrated system.[3,4] This strategy laid an important foundation for the design and construction of multifunctional hybrid DNA hydrogels, and expanded their application scope.[5] However, in current analytical applications, this type of material is limited by its own physicochemical properties and still faces the following key bottlenecks: (1) the signal generation mechanism of DNA hydrogels is deficient at present, resulting in relatively weak signal intensity, which makes it difficult to meet the requirements of practical application scenarios,[6] (2) the molecular biocompatibility and specific recognition capability of hybrid DNA hydrogels are far inferior to those of pure DNA hydrogels (less DNA-carrying capacity),[7] and the reaction kinetics of DNA hydrogels during the detection of target analytes are relatively slow (the diffusion rate of the target object is slow, and so is the probability of collision with the recognition device).[8]

In response to the above bottlenecks, some previous studies[3,9,10] have been conducted. For example, *N*-isopropyl acrylamide (NIPAM) is one of the most commonly used matrix materials for the preparation of temperature responsive hydrogels, mainly due to the ease of adjusting its low critical solution temperature (LCST).[11] However, the lack of hydrophilicity, the limited number of active sites and the ease of phase

[a]School of Materials Science and Engineering, Jiangsu University of Science and Technology, Zhenjiang 212003, Jiangsu Province, PR China. E-mail: tangsheng.nju@gmail.com; chmts@just.edu.cn

[b]School of Environmental and Chemical Engineering, Jiangsu University of Science and Technology, Zhenjiang 212003, Jiangsu Province, PR China. E-mail: wangdongyang@just.edu.cn

[c]Department of Chemistry, National University of Singapore, 3 Science Drive 3, Singapore 117543, Singapore. E-mail: chmleehk@nus.edu.sg; hiankeelee@u.nus.edu

transition at room temperature (the LCST (28 °C) is close to ambient temperature) limits its practical application.[12] In our recent report,[9] the introduction of a strongly hydrophilic acrylamide (AM) monomer for copolymerization modification could not only effectively broaden the LCST range of the NIPAM hydrogel, but also provide more active sites for the loaded DNA, thus improving its hydrophilicity and biocompatibility. To generate detection signals in hybrid DNA hydrogels, some signal probes such as nanoparticles, nanoclusters, nanocrystals, organic molecules, rare earth metals, and aggregation induced emission (AIE) nanomaterials have been reported.[13] AIE nanomaterials stand out due to their high quantum yield and high photostability. When the target chain is introduced into the system, it specifically hybridizes with the probe chain in the gel network, causing a change in the crosslinking density or conformational state of the DNA hydrogel, and thereby triggering a phase transition from sol to gel. This phase transition process leads to a significant contraction of the internal microenvironment of the hydrogel, forming a rigid and relatively hydrophobic nanoscale confined space. Under this confinement effect, the movement of AIE molecules is inhibited, thereby promoting the enhancement of AIE-FL intensity.[14] This enables the attainment of high sensitivity.[6,15] The third bottleneck is also widely present in different types of stimulation-responsive hydrogels, especially in temperature responsive DNA hydrogels.[15] Although a high LCST (much higher than the physiological temperature) can effectively improve the reaction kinetics of DNA hydrogels in recognizing the target,[16] this condition may also destroy the activity of biomolecules and reduce their binding specificity and affinity to the target.[17] Therefore, a highly biocompatible hybrid DNA hydrogel with fast target recognition performance within the physiological temperature window is desired to meet the above three bottlenecks.

Herein, a spatially confined "double-key lock" smart DNA hydrogel has been developed using temperature and miRNA-21 as the double-keys and 1,1,2,2-tetra(4-carboxybenzene) ethylene (TCPE) nanomaterials as the fluorescence (FL) signal probe to achieve target sensitivity to femtomolar (fM) concentrations (Scheme 1, the corresponding explanation can be found in the SI). The DNA cross-linked hydrogel retained the enhanced characteristics of NIPAM hydrogel induced by temperature. The density, LCST and response rate of the hydrogel nanonetwork could be easily adjusted by adjusting the concentration of the DNA cross-linking agent. Furthermore, introducing pivot sequences into linker DNA allowed reversible gelation, ensuring selectivity and dynamic control. Only simultaneous stimulation by temperature and target miRNA can trigger hydrogel network crosslinking contraction and remarkable AIE-FL amplification, forming an AND-type dual-response sensing mode. The DNA hydrogel was successfully used to detect miRNA-21 in serum samples from lung cancer or gastric cancer patients and could also dynamically monitor miRNA-21 secreted by cells, providing an efficient new sensing strategy for tumor marker analysis and clinical translational research. The combination of this thermally responsive NIPAM polymer with a controllably responsive DNA element provided a multifunctional platform with a wide range of potential applications in the biomedical and materials

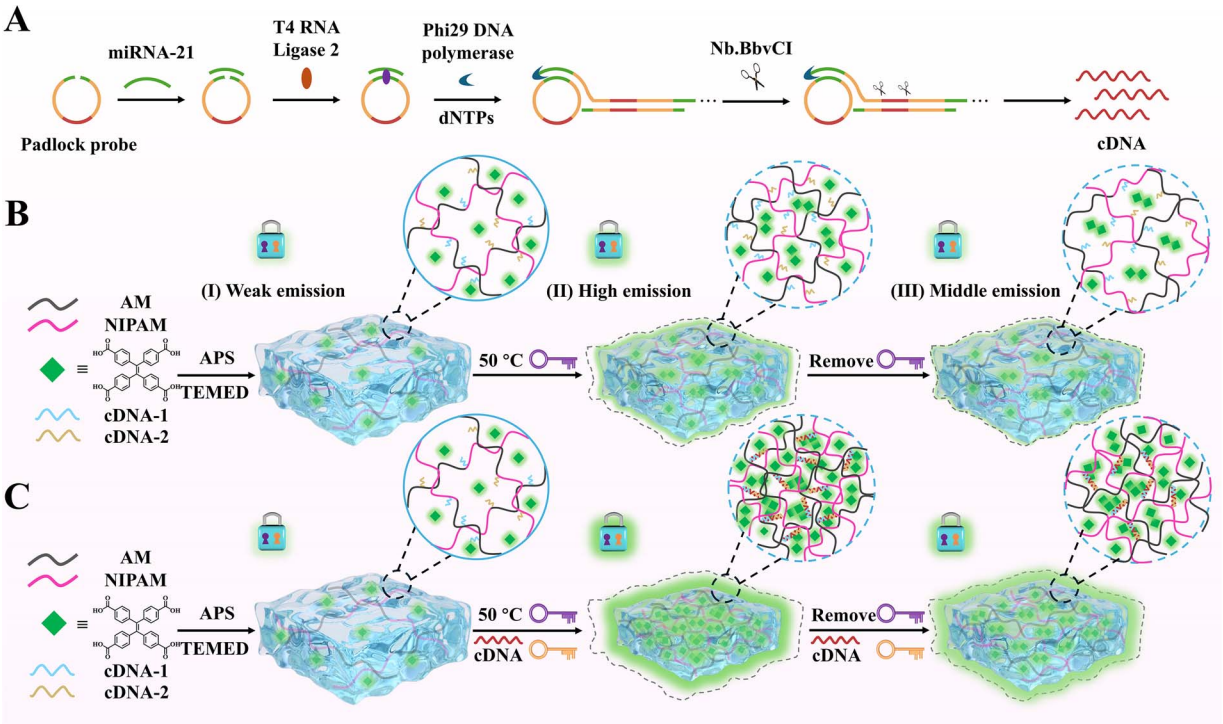

Scheme 1 Schematic of preparation of the "double-key lock" smart DNA hydrogel for detection of miRNA-21. (A) Process of the RCA reaction and (B and C) schematic of the "double-key lock" smart DNA hydrogel response without the target (B), and with the target (C).

science fields. The proposed hydrogel offered several advantages: (1) the DNA components provided excellent biocompatibility and high selectivity at the molecular recognition level through sequence-specific hybridization, minimizing the false non-specific interactions, (2) the temperature-sensitive hydrogel-based sensing platform leveraged its responsive behavior to microenvironmental temperature fluctuations, significantly enhancing detection sensitivity and broadening applicability in complex biological systems, and (3) the smart DNA hydrogel facilitated real-time, *in situ* monitoring of miRNA-21 expression in living cells, providing critical insights for the precise identification of aberrant cellular phenotypes. To the best of our knowledge, few studies have integrated temperature responsiveness with nucleic acid recognition mechanisms for the smart sensing of miRNA and related nucleic acid targets. Notably, the developed "dual-key lock" smart DNA hydrogel principle is not only applicable to the detection of miRNA-21, but can also be used to develop the next generation of intelligent nanosensors for various nucleic acid targets by simply reprogramming the DNA recognition sequence, thus having broad application potential in the field of real-time molecular diagnosis and precision biomedicine.

Results and discussion

Characterization of TCPE

TCPE was synthesized from tetraphenylethylene (TPE) *via* a sequence of bromination, halogen–cyano exchange, reflux reaction, hydrolysis, and gradient column chromatography purification (Fig. 1A).[18] To authenticate the successful synthesis and structural integrity of TCPE, nuclear magnetic resonance (NMR) spectroscopy was employed as a primary characterization tool.[19] The successful synthesis and structural integrity of TCPE were confirmed by ^{1}H and ^{13}C NMR spectra (Fig. S1A and S1B), consistent with previously reported data:[18] ^{1}H NMR (400 MHz, chloroform-d): δ 7.08 (d, J = 8.4 Hz, 8H), 7.72 (d, J = 8.4 Hz, 8H), 12.93 (s, 4H) ppm. ^{13}C NMR (101 MHz, dimethyl sulfoxide-D6): δ 129.67, 129.93, 131.41, 141.70, 146.97, 167.45. According to Fig. 1B, TCPE not only exhibits an obvious UV-vis absorption peak around 296 nm, but also demonstrates bright-cyan FL with a maximum emission wavelength of around 485 nm.[18] To elucidate the AIE characteristics of TCPE, the FL emission intensity was monitored in tetrahydrofuran (THF)/H_2O mixtures with varying H_2O fractions (f_w).[20] As f_w in the THF/H_2O solution increased from 0% to 90%, the FL intensity of the TCPE solution gradually increased. When f_w further increased from 90% to 99%, the FL intensity subsequently decreased at around 485 nm due to concentration quenching *via* aggregation[21] and the formation of non-radiative H-aggregates[22] (Fig. 1C); the mechanism details can be found in the SI. The cyan emission under UV illumination intensified progressively (Fig. S2A), which demonstrated that the FL intensity of TCPE can be enhanced by AIE. These results confirmed that FL enhancement originated from the AIE effect, in which TCPE molecules aggregated in aqueous media, restricting intramolecular rotations and enhancing radiative transitions.[21]

To further demonstrate the correlation between the AIE characteristics of TCPE and molecular aggregation, the morphology of TCPE with f_w = 0% and f_w = 90% was observed using scanning electron microscopy (SEM). When TCPE was dissolved in THF/H_2O solution with f_w = 0%, where the solution consisted primarily of THF, SEM confirmed that TCPE exhibited

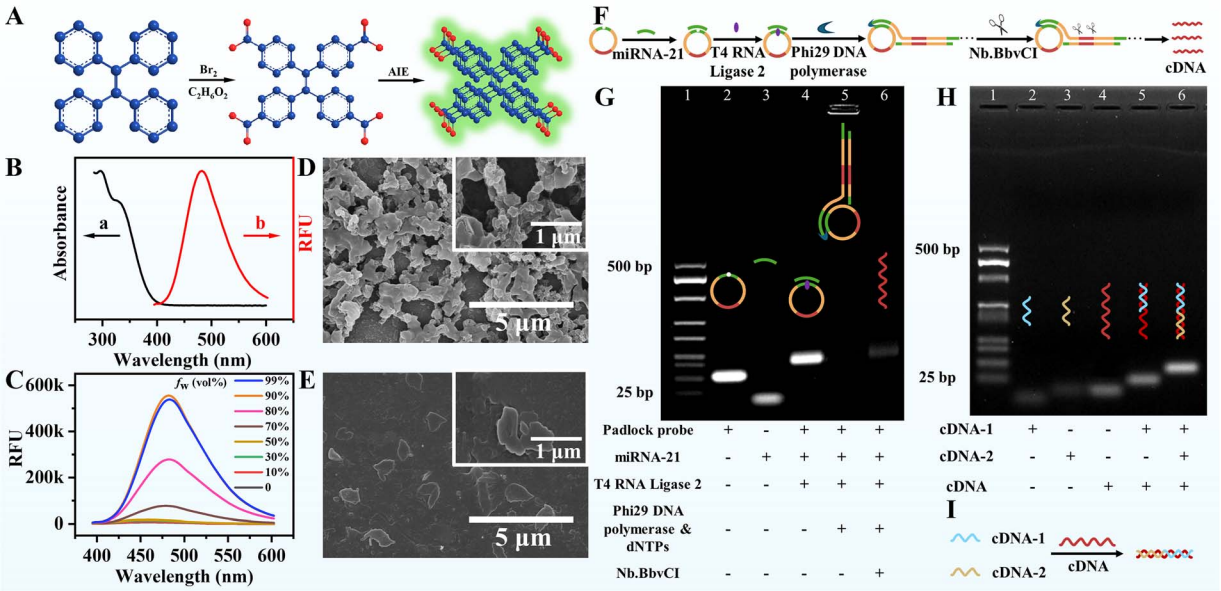

Fig. 1 (A) Schematic of the preparation and AIE process of TCPE. (B) UV-vis absorption (a, black line) and FL emission (b, red line) spectra (e_x = 365 nm) of TCPE. (C) FL spectra of TCPE in THF/H_2O solutions with different f_w values. (D and E) SEM images of TCPE at (D) f_w = 0% and (E) f_w = 90%. (F) Schematic of the RCA reaction process. (G) Agarose gel electrophoresis analysis for the formation of the circular padlock probe. (H) Agarose gel electrophoresis analysis of the reaction between cDNA strands and cDNA. (I) Schematic of the binding reaction between cDNA-1/2 and cDNA.

high crystallinity and uniform distribution (Fig. 1D). In Fig. 1E, the SEM image of the $f_w = 90\%$ solution, where H_2O dominated and acted as a poor solvent, shows no distinct morphology, with irregular shapes and non-uniform distribution. Considering the strong temperature dependence of the preparation of double key lock smart DNA hydrogel, the influence of temperature on the FL of TCPE was explored, as displayed in Fig. S2B. As the temperature increased from 5 °C to 50 °C, FL emission intensity of TCPE showed a gradually decreasing trend. It is worth noting that the FL emission intensity of TCPE showed a significant decrease when the temperature was above 50 °C, mainly attributed to hydrogen bond disruption and thermal dispersion of TCPE molecules.[23]

Design of the smart DNA hydrogel

The temperature-sensitive smart DNA hydrogel was prepared by *in situ* polymerization at 25 °C with NIPAM as the monomer, AM as the functional monomer, cDNA-1/2 as the capture probe, *N*,*N*,*N*′,*N*′-tetramethylethylenediamine as the crosslinker and potassium persulfate as the redox initiator, mixed in water.[24,25] AM, a hydrophilic monomer, served to elevate the lower critical solution temperature (LCST) by adjusting the hydrophilic/hydrophobic balance of the hydrogel matrix.[26] Furthermore, the active amide groups of AM enabled it to participate in typical acrylamide reactions, facilitating covalent bonding with DNA strands.[9] The effect of AM content on LCST of the smart DNA hydrogel was investigated *via* differential scanning calorimetry (DSC) as shown in Fig. S3A. The LCST of the smart DNA hydrogel also increased with the increase in AM contents, indicating that its temperature sensitivity was reduced. This may be because the addition of AM enhanced the content of hydrogen bonds formed between three-dimensional hydrogel and water molecules, thereby increasing the phase transition temperature of the smart DNA hydrogel.[27] Although high temperature was beneficial for shortening the nucleic acid reaction time, temperatures above 50 °C can seriously affect the FL intensity of TCPE. Therefore, AM with a mass fraction w(AM) of 20% was selected for the preparation of the smart DNA hydrogel. At this time, LCST of the smart DNA hydrogel was 40 °C.[17] The contact angle test further verified that AM could be used to improve the hydrophilicity of DNA hydrogels, as demonstrated in Fig. S3B. Compared with NIPAM hydrogel (58.58°), the contact angle of the hydrogel at 25 °C was significantly reduced (33.92°), indicating that AM significantly improved the hydrophilicity of NIPAM hydrogel.[28] When the temperature of the DNA hydrogel increased from 25 °C to 50 °C, the contact angle of the DNA hydrogel increased significantly, indicating that the combination between the hydrogel and water molecules was destroyed by the temperature increase, and volume shrinkage was conducive to the transition from the sol-to-gel state.[28]

Feasibility of the smart DNA hydrogel for target detection

The feasibility of the RCA signal amplification and the subsequent capture of cDNA strands was evaluated using agarose gel electrophoresis. As illustrated in Fig. 1F, the principle of RCA target amplification was first validated. The validation of the RCA reaction is shown in Fig. 1G. Lanes 2 and 3 correspond to the single Padlock probe and target miRNA-21, respectively. Upon co-incubation of the Padlock probe with miRNA-21 in the presence of T4 Rnl2 ligase (lane 4), a new band appeared above the Padlock probe, confirming successful ligation. Subsequent treatment with Phi29 DNA polymerase and dNTPs (lane 5) yielded a high-molecular weight product retained near the loading well, indicating efficient RCA and formation of linear RCA products. Following the introduction of Nb.BbvCI endonuclease, which specifically recognizes and cleaves at the designated sites, multiple short cDNA fragments were generated (lane 6), verifying the visible remnants of the Padlock probe after digestion, with a brighter band above potentially representing a subset of longer RCA products that had been variably cut by the enzyme at different locations. A single band directly proves that the optimized enzymatic digestion reaction can efficiently and uniformly produce the target cDNA fragments. The homogeneity of the RCA products was further validated using high-performance liquid chromatography (HPLC) (Fig. S4).[29] This result clearly demonstrated the successful ligation, and the subsequent efficient execution of the RCA process, leading to the generation of intended products.

The crosslinking effect between capture cDNA-1/2 and cDNA was evaluated by agarose hydrogel electrophoresis, as shown in Fig. 1H. Lanes 2–4 represent the migration bands of cDNA-1, cDNA-2 and cDNA, respectively. A distinct high-molecular-weight band in lane 5 indicates effective hybridization between cDNA-1 and cDNA, while the appearance of a single large band in lane 6 demonstrates the successful formation of a three-way crosslinked network among cDNA, cDNA-1, and cDNA-2. Fig. 1I further illustrates the binding process between cDNA-1, cDNA-2, and cDNA. The key parameters of the loop amplification (RCA) system, including T4 RNA ligase (6 U, Fig. S5A), Phi29 DNA polymerase (2 U, Fig. S5B), dNTPs (5 mM, Fig. S5C), the concentration of the Nb.BbvCI enzyme (10 U, Fig. S5D), and the reaction time (2 h, Fig. S6) for loop amplification, have been optimized. The exploration of the analytical performance and recognition mechanism of the smart DNA hydrogel was carried out under the optimal conditions, and the details can be found in the SI.

Characterization of the smart DNA hydrogel

The preparation of the "double-key lock" smart DNA hydrogel was tracked in detail through circular dichroism (CD)[30] and Fourier transform infrared (FTIR),[31] UV and FL spectroscopy studies to verify the interaction mechanism between the hydrogel, TCPE and cDNA-1/2.[32] CD spectroscopy was first used to demonstrate the specific binding ability of the cDNA to cDNA-1 and cDNA-2 as shown in Fig. 2A. The cDNA has a peak at 277 nm. The mixed system of cDNA-1 and cDNA-2 exhibits a characteristic absorption peak at 274 nm corresponding to the intrinsic CD signal of the double stranded nucleic acid structure. After the cDNA was added to the mixed system of cDNA-1 and cDNA-2, the position of the peak was red shifted. The peak appears in the figure at about 280 nm, indicating that cross-

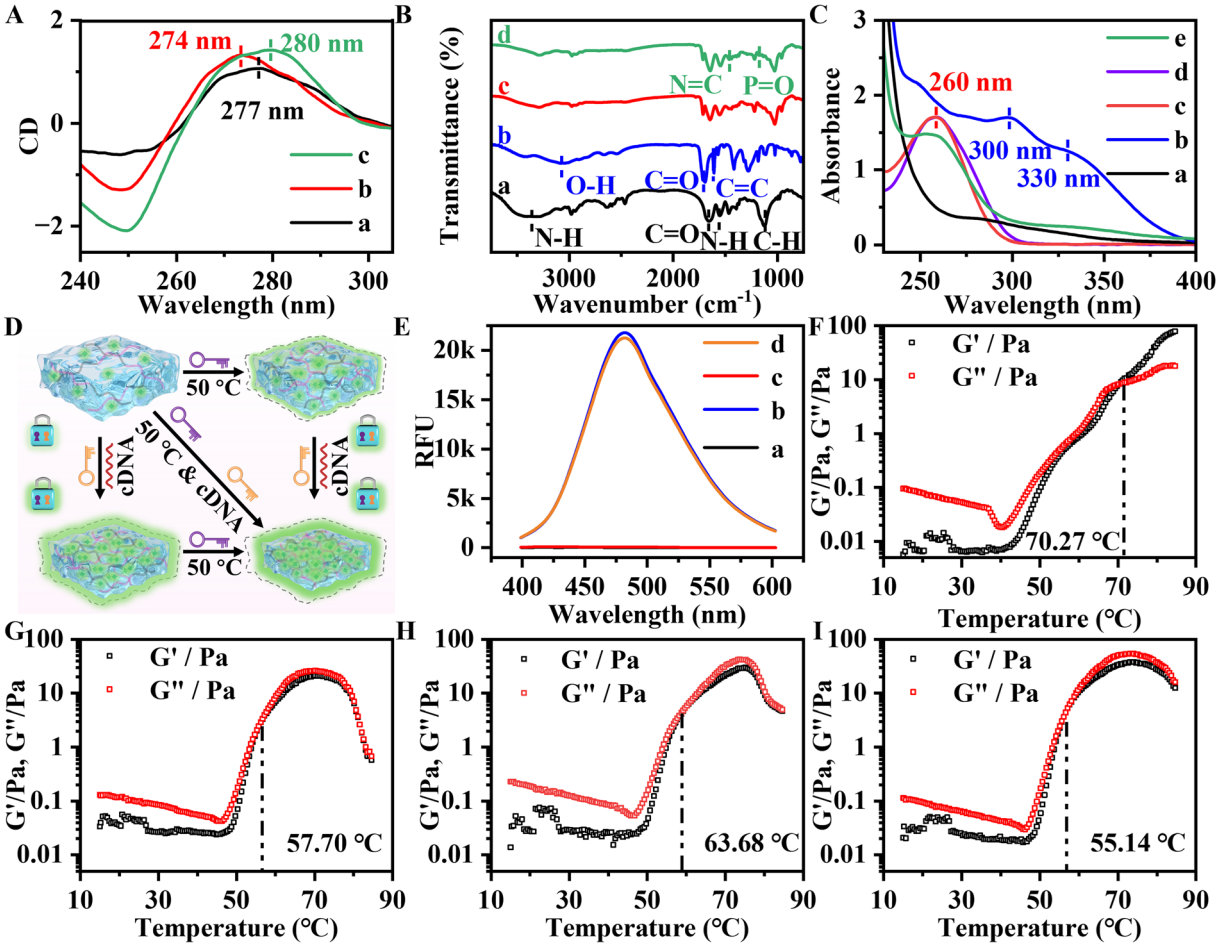

Fig. 2 (A) CD spectra of (a) cDNA, (b) cDNA-1 + cDNA-2, (c) cDNA-1 + cDNA-2 + cDNA. (B) FTIR spectra of (a) hydrogel, (b) TCPE, (c) TCPE-hydrogel, (d) TCPE-hydrogel-cDNA-1/2. (C) UV-vis absorption of (a) hydrogel, (b) TCPE, (c) cDNA-1, (d) cDNA-2, and (e) smart DNA hydrogel. (D) Schematic of the smart DNA hydrogel used to detect miRNA-21 under different temperature and cDNA conditions. (E) FL spectra of (a) hydrogel, (b) TCPE, (c) cDNA-1 and (d) smart DNA hydrogel. (F–I) Temperature sweep test of the smart DNA hydrogel (F and G) without cDNA at (F) 25 °C and (G) 50 °C, and (H and I) with cDNA at (H) 25 °C and (I) 50 °C.

linking occurred between cDNA-1 and cDNA-2 through cDNA.[30,33] In Fig. 2B, the FTIR spectrum of the hydrogel shows a characteristic peak at 1641 cm^{-1}, due to the stretching vibration of C=O in the amide group (curve a).[34] The N–H bending vibration in amide is observed at 1550 cm^{-1}, while the broad peak from 2500 to 3300 cm^{-1} is due to O–H stretching vibration. The broad peak at 3000 to 3500 cm^{-1} centered at 3434 cm^{-1} can be attributed to the amide bond ($-CONH_2$). The FTIR spectrum of TCPE confirms the presence of a large number of carboxyl groups (curve b).[35] The FTIR spectrum of the TCPE-hydrogel (curve c) fails to exhibit the characteristic absorption peak of TCPE, which is primarily attributed to the deep embedding of TCPE within the hydrogel network, where its characteristic absorption peaks were masked by the strong absorption signals of the hydrogel matrix and water molecules (such as the wide O–H peak). In addition, the characteristic absorption peaks corresponding to the hydrogel shows a red shift, indicating that a dehydration condensation reaction occurred between TCPE and the hydrogel, connecting them together. The introduction of acrylamide-modified cDNA-1 and cDNA-2 was confirmed by a peak at 1455 cm^{-1} corresponding to N=C stretching in the adenine moiety and at 1172 cm^{-1} for P=O stretching, verifying the covalent attachment of cDNA-1 and cDNA-2 to the hydrogel.[36] According to Fig. 2C, the UV-vis spectrum of the hydrogel does not show any obvious characteristic absorption peak (curve a). TCPE exhibits two weak characteristic absorption peaks near 296 nm and 335 nm (curve b), while the characteristic peaks of cDNA-1 (curve c) and, cDNA-2 (curve d) are both located around 260 nm. The pretreated "double-key lock" smart DNA hydrogel (curve e) displays obvious characteristic peaks of cDNA-1/2 at 260 nm, confirming the successful conjugation of cDNA-1 and cDNA-2 to the hydrogel matrix.

Subsequently, a FL strategy was used to validate the construction of the "double-key lock" smart DNA hydrogel and its feasibility for miRNA detection.[37] The specific schematic is shown in Fig. 2D. According to Fig. 2E, the DNA hydrogel and cDNA-1 both do not exhibit any obvious FL signal. The smart DNA hydrogel displays a FL peak similar to that of TCPE around 485 nm, indicating that the influence of the hydrogel on the FL

characteristics of TCPE can be ignored. In Fig. S7, the smart DNA hydrogel at 25 °C (curve b) shows a weaker FL signal than pure TCPE at 485 nm (curve a). After the temperature was raised from 25 °C to 50 °C, the FL signal of the smart DNA hydrogel was found to increase significantly (curve c), attributable to the fact that 50 °C was higher than the LCST (40.35 °C) of the smart DNA hydrogel, and the aggregation degree of TCPE molecules increased with the change in the hydrogel state, thus enhancing the FL intensity. After adding cDNA to the "double-key lock" smart DNA hydrogel at 25 °C (curve d), the FL peak around 485 nm was found to significantly increase by 5 times compared to the original (curve b). This phenomenon can be explained by the fact that the pore diameter of the hydrogel was reduced after adding cDNA, which caused the monodispersed TCPE to aggregate, further enhancing its FL intensity. Similarly, after the temperature of this mode was raised to 50 °C, the FL peak of the smart DNA hydrogel was found to further increase. Therefore, the sensitivity of the smart DNA hydrogel can be greatly improved by using temperature and cDNA as two keys. Upon reverting to 25 °C, the FL signal experienced a slight reduction yet remained notably higher than the initial level. This suggests that although the hydrogel underwent a reversible transition back to a sol state below its LCST, the inter-cDNA connections maintained the hydrogel in a contracted state, with TCPE remaining primarily aggregated.

The viscoelastic properties and network architecture of the smart DNA hydrogel were characterized as a function of temperature and cDNA concentration by frequency-sweep rheological measurements of the G' and G'' (Fig. 2F–I),[34] (where G' represents the elasticity of the hydrogel, and G'' reflects the viscosity of the hydrogel). According to Fig. 2F and G, the phase transition temperatures of smart DNA hydrogels without cDNA at 25 °C and 50 °C are 70.27 °C and 57.70 °C respectively, indicating that the rising temperature drove the phase structure of the hydrogels to change from "discrete droplets" to "continuous networks".[38] Fig. 2H and I demonstrates that the phase transition temperatures of smart DNA hydrogels with cDNA at 25 °C and 50 °C are 60.68 °C and 55.14 °C respectively, indicating that the continuity and density of hydrogel networks were enhanced by the interaction between cDNA and cDNA-1/2 through base complementary pairing, ultimately improving the elastic modulus and thermal stability.[24]

To visually verify the influence of temperature and target cDNA on the analytical performance of the prepared "double-key lock" smart DNA hydrogel (Fig. 3A), the hydrogels with or without cDNA were freeze-dried with liquid nitrogen at 25 °C or 50 °C to maintain their original morphology, and their phases were observed by SEM and FL confocal microscopy. As shown in Fig. 3B, the hydrogel without cDNA at 25 °C exhibits a large layered porous microstructure, in which the walls of the pores were thick and rough. After the temperature was raised from 25 °C to 50 °C, the internal pore size of the hydrogel was slightly reduced (Fig. 3C). After adding cDNA, it was observed that the pore size of the water coagulation decreased significantly (about 70 μm), while the walls of the pores became thinner and rougher (Fig. 3D). Compared with the first three states, the pore

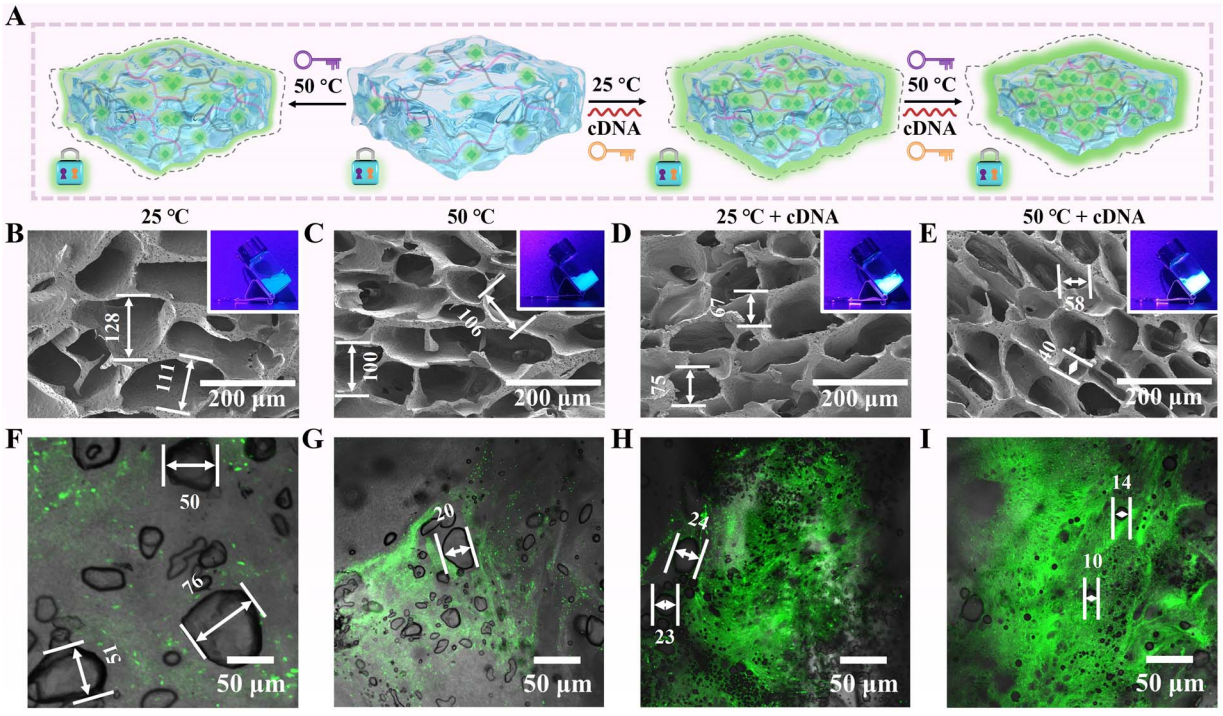

Fig. 3 (A) Schematic of the influence of temperature and cDNA on the smart DNA hydrogel performance. (B–E) SEM of the smart DNA hydrogel without cDNA at (B) 25 °C and (C) 50 °C, and with cDNA at (D) 25 °C and (F) 50 °C. (F–I) FL confocal microscopy images of the smart DNA hydrogel without cDNA at (F) 25 °C and (G) 50 °C, and with cDNA at (H) 25 °C and (I) 50 °C. The inset of (B–E): FL photographs of the corresponding states.

size of the hydrogel was smaller and denser, and the pore walls were rougher (Fig. 3E). This clearly demonstrates that temperature and cDNA had a significant impact on the ability of hydrogels to shrink.[39] Fig. S8 and the inset of Fig. 3B–E further verify the influence of temperature and cDNA on the FL performance of the "double-key lock" smart DNA hydrogel. Fig. S8 displays the photographs of hydrogels prepared under different conditions, which further proves that temperature and cDNA can change hydrogels from a sol-state to a gel-state. The smart DNA hydrogel without cDNA was transparent at 25 °C. The strategy of increasing the temperature or adding cDNA can reduce the transparency and shrink the volume of the smart DNA hydrogel. The smart DNA hydrogel with cDNA was opaque at 50 °C. Compared with the hydrogel in other states, the hydrogel in this state showed the smallest transparency and the largest volume shrinkage. Similarly, the illustration in Fig. 3B–E clearly proves that with the increase in temperature and the addition of cDNA, the volume shrinkage of the hydrogel was the largest and the FL intensity was the strongest.

The effects of temperature and cDNA on the phase behavior, FL distribution and gel process of smart DNA hydrogels were systematically studied by FL confocal microscopy. The smart DNA hydrogel without cDNA at 25 °C showed weak FL intensity and a scattered distribution, indicating that TCPE was distributed more discretely and had a lower degree of aggregation in this system (Fig. 3F). It is worth noting that the hydrogel showed vesicle-like pores with a size of about 70 μm. When the smart DNA hydrogel was heated to 50 °C (Fig. 3G) or cDNA was added (Fig. 3H), the size of the pores resembling vesicles gradually decreased, while their number increased. In addition, FL brightness was significantly improved and showed a uniform regional distribution, indicating that increasing the temperature or adding cDNA could promote the phase transformation of three-dimensional network structure of the hydrogel, thereby enhancing the degree of aggregation of TCPE. As expected, the smart DNA hydrogel with cDNA at 50 °C (Fig. 3I) displayed not only continuous green FL, but also high brightness, dense distribution, and even a FL "clustering" effect. This phenomenon can be explained as follows: the synergistic effect of temperature at 50 °C and cDNA could induce the phase separation of the hydrogel and intensify the formation of a highly cross-linked, dense three-dimensional network.[20] Therefore, temperature and cDNA as double keys can improve the sensitivity of the smart DNA hydrogels.[40]

Theoretical simulation analysis and the mechanism of smart DNA hydrogel for miRNA detection

To better understand the influence of temperature and cDNA on the aggregation process of the hydrogel and TCPE, molecular dynamics simulations (MDs) were carried out (Fig. 4A).[31,41] The model structures in the MDs were obtained using an open source visualization tool.[42] Four samples, namely the smart DNA hydrogel samples before and after recognition of cDNA at 298 K (25 °C) and 323 K (50 °C), were used for subsequent simulation experiments.[43] To ensure that the model in every state was fully relaxed, each was simulated for 10 s. The relaxation videos of the four states of materials (the smart DNA hydrogel (Movie S1) without and (Movie S2) with cDNA at 25 °C, and the smart DNA hydrogel (Movie S3) without and (Movie S4) with cDNA at 50 °C) correspond to Movies S1–S4, respectively. For each DNA hydrogel model within the first 2 s, it was observed that the initial randomly dispersed molecules (Fig. S9) rapidly gathered into dense three-dimensional porous network nanoclusters (Fig. 4B–E). In Fig. 4B–E, the volumes of the four models aggregated from the same initial volume are shown as 103.71^3, 87.31^3, 91.85^3 and 97.07^3 respectively. It is evident that, the smart DNA hydrogel exhibited the most significant volume contraction compared to other models under the influence of temperature and cDNA. It is worth noting that the MDs primarily provide atomistic insights into local stiffening mechanisms, such as crosslinking density evolution or confined water behavior, rather than a direct representation of macroscopic syneresis. For more details about the MDs, please refer to the SI. Meanwhile, the TCPE molecules were affected by spatial regions, resulting in the greatest degree of aggregation (Fig. S10). Fig. S11A and S11B demonstrate that hydrogen bonds, van der Waals, and electrostatic interactions are the key interaction forces driving conformational changes in DNA hydrogels in the four model systems. Compared with other hydrogel models, the smart DNA hydrogel with cDNA at 323 K shrank the most in the same time. Therefore, TCPE molecules exhibited the highest degree of aggregation and FL intensity under the action of these forces.

For mean square displacement (MSD) and diffusion coefficients calculations (DCC), to collect dynamic trajectories for subsequent data analysis, the different systems were simulated at 298 K/323 K and 1 atm for 20 ns under the isothermal–isochoric NVT ensemble using a velocity-rescale thermostat with a time step of 1.0 fs.[44] In Fig. S11C, the slope of the curve reflects the rate of diffusion of TCPE molecules. The differences in MSD growth among different models intuitively demonstrated the degree of restriction imposed by the microstructure of the four models on the motion of TCPE molecules. Due to the synergistic effects of temperature and cDNA, the DNA hydrogel had a dense three-dimensional network structure, which caused the MSD of TCPE molecule to be relatively slow. The quantitative characterization of the diffusion coefficient directly reflected the diffusion ability of TCPE molecules in different models (Fig. S11D), which is consistent with the MSD results.

The mechanism underlying the influence of temperature and cDNA on the performance of the smart DNA hydrogel is depicted in Fig. 4F. At a temperature (25 °C) < LCST of the hydrogel, strong hydrogen bonds were formed between the hydrophilic group (hydroxyl or amino) in the hydrogel chain and the surrounding water molecules, which enabled the hydrogel polymer to be well dissolved in water. Therefore, the FL intensity of the hydrogel was weak. This is mainly because the distance between TCPE molecules was far greater than the critical aggregation distance required for the AIE effect, the intramolecular movement (rotation and vibration) was not limited, and the AIE-FL effect was suppressed, resulting in the weak FL intensity of the hydrogel. At a temperature (50 °C) > LCST of the hydrogel, the hydrogen bonds were destroyed, and

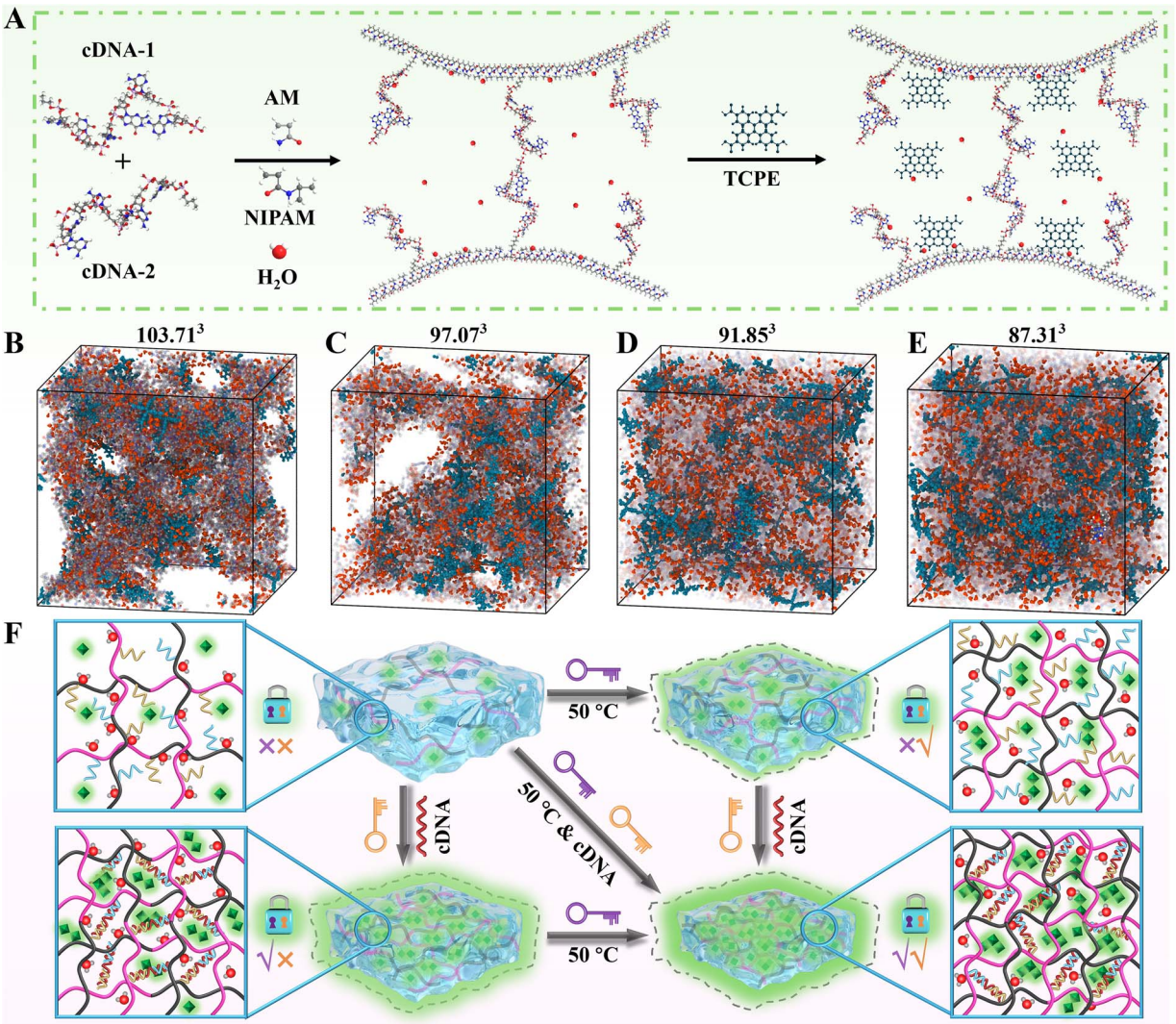

Fig. 4 (A) Schematic of the process of preparing the smart DNA hydrogel by cross-linking NIPAM, AM, cDNA-1/2 and water molecules. (B–E) MDs of the smart DNA hydrogel after running for 10 s. Initial MDs without cDNA at (B) 25 °C and (C) 50 °C, and with cDNA at (D) 25 °C and (E) 50 °C. (F) Schematic of the mechanism underlying the influence of temperature and cDNA on the "double-key lock" smart DNA hydrogel.

the interaction between hydrophobic groups and the formation of intramolecular hydrogen bonds became dominant, leading to a transition of hydrogels from an "initial loose macroporous structure" to a "dense mesoporous network". At the same time, TCPE gradually gathered together under the influence of spatial confinement during the shrinkage of the hydrogel, leading to the gradual enhancement of FL intensity. After the addition of cDNA at 25 °C, the cDNA further induced the cross-linking and conformational changes of the hydrogel molecular chains by specifically binding to the pre modified cDNA-1/2 in the hydrogel through base complementary pairing. At this time, the distance between TCPE molecules was further shortened with the shrinkage of the hydrogel, and the degree of aggregation was significantly increased, thus enhancing the FL intensity of TCPE. When high temperature synergized with cDNA, the thermal stimulation at 50 °C provided a "kinetic drive" by breaking hydrogen bonds and enhancing hydrophobic interactions, while cDNA was recognized as "structure oriented" by specific molecules through base complementary pairing. The two phenomena synergistically triggered the conformational change in the DNA hydrogel to form the densest three-dimensional network structure, with further shrinkage of the pore size. In this process, the AIE type TCPE probe aggregated extremely efficiently with the network densification driven by the hydrogel, thus maximizing the AIE-FL effect of TCPE and maximizing the FL intensity of the hydrogel.

Optimization of experimental conditions

To achieve optimal sensing performance, various experimental conditions related to this strategy were evaluated, including the concentrations of cDNA-1 and cDNA-2, TCPE concentration, pH of buffer, reaction temperature and reaction time of cDNA. Fig. S12A illustrates that the FL signal of the "double-key lock" smart DNA hydrogel gradually increases with the increases in cDNA-1 and cDNA-2 concentrations. When the concentration of cDNA-1

and cDNA-2 was 100 μM, the FL signal was optimal. This phenomenon can be explained as follows: when the concentration of cDNA-1 and cDNA-2 was lower than 100 μM, a large amount of cDNA was free in the hydrogel, which was not conducive to phase separation within the hydrogel, and the signal of TCPE was weak. With the increase in the concentration of cDNA-1 and cDNA-2, the hydrogen bonding force inside the hydrogel increases, and the aggregation of TCPE increases, thus further enhancing the FL signal. Fig. S12B illustrates an increase in signal intensity with increasing TCPE concentration, stabilizing at 1 mM as the optimal concentration. Given the acidic nature of TCPE due to its four carboxyl groups, the buffer pH influenced its molecular structure and thus, its luminescence properties. To determine the optimal reaction pH, the FL signal amplification effect of the reaction system was analyzed in buffer solutions with pH values ranging from 5.0 to 10.0. The results indicated that a pH of 7.0 provided the optimal condition for this method (Fig. S12C). Fig. S12D and S12E show the optimal reaction temperature and time for DNA to be 50 °C and 80 min, respectively.

Performance analysis of the "double-key lock" smart DNA hydrogel

As presented in Fig. 5A, when "double-key lock" smart DNA hydrogels were fabricated using target miRNA-21 samples of different concentrations, all sensing systems exhibited similar FL emission profiles, with the maximum FL emission wavelength centered at ~485 nm. The maximum FL intensity of the "double-key lock" smart DNA hydrogel sensing system exhibited a dose-dependent increase with the concentration of the target miRNA-21 (curves a–j). The linear relationship between the maximum FL intensity and the logarithm of target miRNA-21 concentration ranges from 0.1 fM to 10 nM (inset of Fig. 5A). This sensing system can be used for sensitive determination of target miRNA-21 with a limit of detection (LOD) of 33.3 aM at

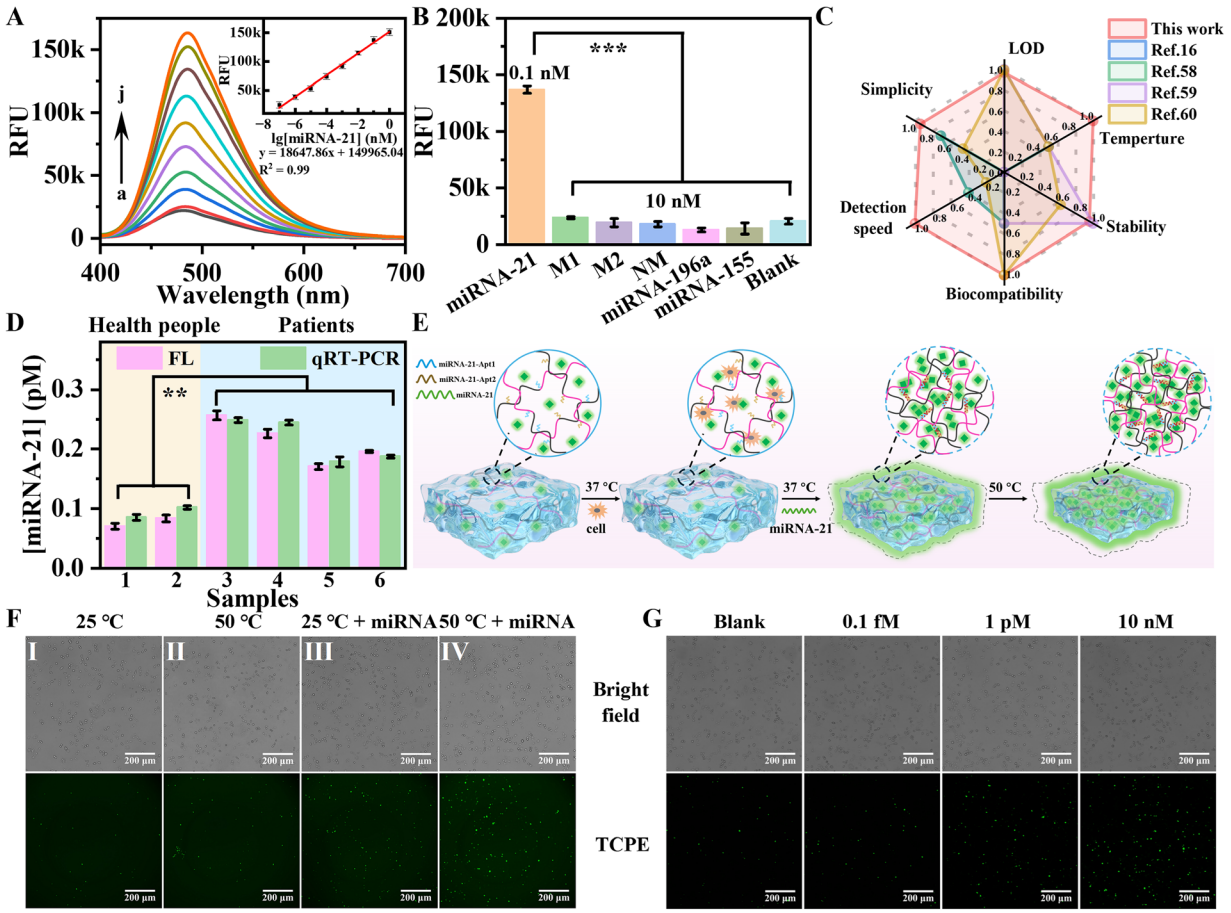

Fig. 5 (A) FL intensity profiles of the "double-key lock" smart DNA hydrogel formed with 10 μL of (a) blank and (b) 0.1 fM, (c) 1 fM, (d) 10 fM, (e) 100 fM, (f) 1 pM, (g) 10 pM, (h) 100 pM, (i) 1 nM, and (j) 10 nM miRNA-21. (B) Specificity analysis of this strategy towards miRNA-21 and various other targets, with miRNA-21 at 0.1 nM and others at 10 nM. (C) Radar chart comparing the proposed hydrogel with previously reported DNA hydrogels. (D) A comparative diagram illustrating the relative expression level of miRNA-21 in serum samples of healthy individuals and patients determined by this method (pink) and the real-time quantitative polymerase chain reaction (RT-qPCR) method (green). The results are expressed as means ± SD of three replicates. Statistical analysis was performed using one-way analysis of (C) variance and (D) *T*-test. Asterisks indicate the level of significance (**$p < 0.01$, and ***$p < 0.001$). (E) Schematic of the DNA hydrogel used for dynamic detection of miRNA-21 secreted by cells. (F) FL micrographs of four hydrogel models containing MDA-MB-231 cells incubated with 10 nM miRNA-21 for 12 h. (G) FL micrographs of the smart DNA hydrogel containing MDA-MB-231 cells incubated with 0 nM (PBS), 0.1 fM, 1 pM, and 10 nM miRNA-21 for 12 h. The inset of (A): the corresponding calibration curve for target miRNA-21 determination.

a signal-to-noise ratio of 3 (S/N = 3). The major characteristics of some other strategies used for miRNA detection were compared with our proposed strategy (Table S2).[45–49] The proposed smart DNA hydrogel has a wide linear range and a low LOD, which allows the detection of miRNA-21 in healthy cells (approximately 1 pM) and cancer cells (approximately 5 pM).

Ensuring specificity in the sensing system to recognize mismatched base pairs was crucial for accurate nucleic acid analysis. Therefore, the specificity of the proposed the "double-key lock" smart DNA hydrogel for miRNA was determined by using common nucleic acids as controls, including the single base mismatch (M1), double base mismatch (M2), and unpaired sequence (NM) of miRNA-21, as well as miRNA-196a and miRNA-155. As shown in Fig. 5B, the "double-key lock" smart DNA hydrogel prepared using the samples with a concentration 100 times (10 nM) higher than that of miRNA-21 (0.1 nM) failed to exhibit any significant FL response, similar to the blank. This result clearly confirmed the excellent selectivity and detection specificity of the proposed sensing strategy, which effectively resists interference from structurally homologous miRNAs. Consequently, the system can accurately distinguish target miRNAs from homologous sequence disruptors in serum samples. Additionally, reproducibility was studied by preparing six different smart DNA hydrogels to detect miRNA as shown in Fig. S13. The results reveal that the proposed strategy possessed satisfactory repeatability with a relative standard deviation (RSD) of ± 2.2%. The developed smart DNA hydrogel was compared with previously reported hydrogels to demonstrate its advantages according to multiple analytical performance indicators. As presented in Fig. 5C, the smart DNA hydrogel has excellent performance in terms of LOD, detection speed, biocompatibility, simplicity, *etc.*[25,50–52] These characteristics indicated the reliability and accuracy of the developed "double-key lock" smart DNA hydrogel for the dynamic detection of miRNA-21 secreted by cells.

Analysis of real samples

To evaluate the feasibility and accuracy of the proposed strategy in actual samples, six human serum specimens containing different concentrations of miRNA-21 including two healthy volunteers, two lung cancer patients, and two gastric cancer patients with gastric cancer (from the local tertiary hospitals) were employed to verify the accuracy of this method with the standard addition method. As demonstrated in Table S3, the detection recovery ranges from 97.4% to 104.5% with RSD values of 1.3% to 4.1%. It is noteworthy that miRNA-21 levels of 0.047 pM and 0.048 pM were detected in the serum samples from the two healthy volunteers, whereas significantly higher concentrations of miRNA-21 were identified in the serum of both lung and gastric cancer patients.[50,53] This result demonstrates that miRNA-21 can serve as a biomarker for cancer diagnosis.[25] For comparison, the same samples were also detected using a commercial kit based on qRT-PCR. According to Fig. 5D, the results obtained using the proposed sensing strategy for miRNA-21 were consistent with those from the qRT-PCR method, indicating that the proposed strategy holds great promise for determining miRNA-21 in real samples.

In addition, the proposed "double-key lock" smart DNA hydrogel was used to dynamically monitor miRNA-21 in various cells including healthy cells (LX2 cells) and cancer cells (MDA-MB-231 cells and Hela cells) to further verify its potential practical value. The detection mechanism diagram is illustrated in Fig. 5E. Firstly, the cytotoxicity of the smart DNA hydrogel was evaluated using the MTT assay to examine the growth and survival status of cells within the hydrogel system.[54] As shown in Fig. S14, compared with the PBS control group, the smart DNA hydrogel exhibited lower toxicity towards the LX2, MDA-MB-231 and Hela cells with cell viability maintained at a high level, indicating that the hydrogel possesses good biocompatibility. Further analysis of the effect of temperature on cell activity revealed that compared with 37 °C culture conditions, the treatment at a low temperature (25 °C) had a smaller impact on the cell survival rate, and the cells still maintained high metabolic activity, while the treatment at a high temperature (50 °C) significantly inhibited cell activity, resulting in a significant decrease in the cell survival rate. Although high temperature (50 °C) may cause certain damage to cells, the MTT experiment results show that high-temperature conditions have a limited impact on the cell survival rate. Moreover, after 24 h of normal culture at 37 °C, the miRNA secreted by the cells was detected using the smart DNA hydrogel. At this point, the miRNA had been fully released by the cells during the previous incubation process and had been enriched in the smart DNA hydrogel. Therefore, the detection results obtained under high-temperature conditions can accurately reflect the true miRNA expression level of the cells, further highlighting the advantages of this hydrogel system in dynamic monitoring. These results demonstrate that the constructed smart DNA hydrogel has excellent cell compatibility under physiological temperature and sub-physiological temperature conditions.

Fig. 5F and S15–S17 provide the imaging performance of the smart DNA hydrogel for miRNA-21 secreted by MDA-MB-231 (Fig. 5F and S15), LX2 (Fig. S16) and HeLa cells (Fig. S17) under the synergistic influence of temperature and miRNA-21.[55] The FL intensity of the smart DNA hydrogel at 37 °C in the presence or absence of the target (Fig. S15) was similar to that at 25 °C (I and III in Fig. 5F). This indicates that the physiological temperature (37 °C) is not an essential factor for activating the key part of the double bond lock system to respond, and it does not affect the detection specificity and accuracy of this hydrogel. Compared with the first three groups, the smart DNA hydrogel can improve the FL intensity of the smart DNA hydrogels, *i.e.*, sensitivity, under the double synergistic effect of temperature and miRNA-21. It is worth noting that even at low temperatures and without the addition of miRNA-21, the smart DNA hydrogels can still recognize the trace amounts of miRNA-21 secreted by cells. Next, the analytical performance of smart DNA hydrogels was studied by controlling the content of miRNA-21. Smart DNA hydrogels were treated with different concentrations of miRNA-21 (blank, 0.1 fM, 1 pM and 10 nM) according to the standard addition method (Fig. 5G). The FL background observed in the control group was attributed to the miRNA-21

secreted by MDA-MB-231 cells, indicating that cells can normally survive in the prepared smart DNA hydrogel. The addition of different concentrations of miRNA-21 also led to a significant dose-dependent increase in FL intensity in the hydrogel. This enhancement was due to the higher level of miRNA-21, which led to an increase in the aggregation of TCPE in the hydrogel. The imaging results showed that the concentration of miRNA-21 secreted by MDA-MB-231 cells was approximately 0.32 pM after calculation. Therefore, the proposed sensing strategy can be used for imaging and dynamic monitoring analysis of miRNA-21.

Experimental

Preparation of TCPE

TCPE was successfully prepared according to the reported method.[18] The specific steps were as follows: tetrabromo tetraphenylethylene (TPE-Br_4) was obtained from tetraphenylethylene (TPE) through a bromination reaction. Subsequently, a mixture of TPE-Br_4 and cuprous cyanide in anhydrous DMF were refluxed for 72 h under nitrogen. Subsequently, ethylenediamine and H_2O were added to the above system at 90 °C, and stirred for 3 h to complete the halogen cyanide exchange reaction. The system was then treated with KOH and ethylene glycol, followed by a 72 h reflux. Finally, the reaction system was subjected to hydrolysis treatment, hydrochloric acid acidification, and chromatographic purification at ambient temperature to obtain the light-yellow solid product TCPE.

Rolling circle amplification process

Firstly, a mixture of 10 μL of 20 μM Padlock probe and target miRNA was heated at 65 °C for 3 min. Then, the mixture was placed on ice for 2 min and stored at −20 °C. Subsequently, 2 μL of 20 μM Padlock probe/miRNA substrate, 2 μL of 10 × T4 RNA Ligase 2 (T4 Rnl2) reaction solution, 4 μL of 50% PEG8000 solution, 1.6 μL of 100 mM $MgCl_2$, and 1 μL of T4 Rnl2 (10 U) were mixed with 9.4 μL of deionized H_2O and incubated at 37 °C for 1 h to obtain the ligation reaction product. Then, 10 μL of the ligation reaction product was mixed with 2 μL of 10 × Phi29 DNA polymerase reaction buffer, 2 μL of 10 mM dNTPs, 1 μL of 10 U per μL Phi29 DNA polymerase, and 5 μL of H_2O, and reacted at 30 °C for 2 h to obtain the rolling circle amplification (RCA) product (Scheme 1A). Finally, the RCA products were purified using commercially available DNA purification kits to remove any residual substances that might affect the subsequent experiments.[56]

Preparation of the smart DNA hydrogel for the detection of extracellular miRNA-21

The smart DNA hydrogel was prepared according to a previously reported method by our research group.[9] NIPAM (3 g) and 0.75 g of acrylamide (AM) were sequentially added to 30 mL of H_2O and sonicated for 10 min. Then, 1 g of ammonium persulfate and 1 mL of *N*,*N*,*N*′,*N*′- tetramethylethylenediamine were successively added to the mixed solution and ultrasonicated at ambient temperature for 20 min to obtain solution A. TCPE (1 mM, 200 μL) and 200 μL of 50 mg per mL *N*-hydroxysuccinimide (NHS) and 1-ethyl-3-(3-dimethylaminopropyl) carbodiimide hydrochloride (EDC) solution were mixed for 30 min to activate the carboxyl group in TCPE to obtain solution B. Then, 400 μL of solution A, 200 μL of solution B, 10 μL 100 μM of cDNA-1 and cDNA-2 were mixed with 390 μL of PBS and sonicated at room temperature for 30 min to obtain a TCPE@-NIPAM–AM hydrogel with a three-dimensional network structure; this was designated as the spatially confined "double-key lock" smart DNA hydrogel. This hydrogel was immersed in buffer solution at least five times to thoroughly remove unreacted impurities, including free cDNA, salts, *etc.* This system was used for the detection of extracellular miRNA-21. Finally, the RCA product was introduced into this hydrogel system and incubated at 50 °C for 1 h. Under these conditions, the RCA product and the cDNA in the hydrogel triggered the aggregation of TCPE molecules through a hybridization reaction, thereby generating a strong FL signal and enabling the sensitive detection of the target miRNA. Schemes 1B and 1C illustrate the mechanism of the "double-key lock" smart DNA hydrogel used for detecting miRNA-21 in the absence (B) and presence (C) of the target.

Preparation of smart DNA hydrogel for the detection of miRNA-21 secreted by cells

NIPAM (3 g) and 0.75 g of acrylamide (AM) were sequentially added to 30 mL of H_2O and sonicated for 10 min. Then, 1 g of ammonium persulfate and 1 mL of *N*,*N*,*N*′,*N*′-tetramethylethylenediamine were successively added to the mixed solution and ultrasonicated at ambient temperature for 20 min to obtain solution A. TCPE (1 mM, 200 μL) and 200 μL of 50 mg per mL NHS and EDC solution were mixed for 30 min to activate the carboxyl group in TCPE to obtain solution B. Then, 400 μL of solution A, 200 μL of solution B, 10 μL of 100 μM miRNA-21-Atp1 and miRNA-21-Atp2 probes were mixed with 390 μL of PBS and sonicated at room temperature for 30 min to obtain the "double-key lock" smart DNA hydrogel. This system is used for the detection of miRNA-21 secreted by cells. Finally, the cell suspension and hydrogel precursor solution were mixed rapidly and gently using a pipette under ice-cold conditions, and the mixture was subsequently transferred to a sterile culture plate. Static culture was carried out at 37 °C in a 5% CO_2 incubator for 24 h to establish a stable cell–hydrogel composite system.

Actual serum sample pre-treatment

For genuine sample analysis, serum samples from healthy volunteers, lung cancer patients, and gastric cancer patients were obtained from the local hospital. All experiments were performed in accordance with the Guidelines Ethical Review of Biomedical Research Involving Human Subjects, and approved by the ethics committee at Affiliated Hospital of Jiangsu University (accreditation number: KY2021K0908). Informed consent was obtained from human participants of this study. Serum samples were centrifuged at 12 000 rpm for 10 min at 4 °C to collect the supernatant as the test solution, without any

pre-treatment steps such as dilution or extraction.[57] Subsequently, equal volumes of clarified serum were added to exogenous miRNA-21 standard solutions (0, 0.5 and 5 pM) to form a concentration gradient. Then, RCA reactions were performed on serum samples containing different concentrations of miRNA-21 to obtain cDNA products corresponding to each concentration gradient. The experiments were repeated at least three times under strictly controlled reaction conditions. Finally, the background content of endogenous miRNA-21 in the serum samples was calculated using the calibration curve. Similarly, other interfering substances were subjected to RCA and used to validate the selectivity of the proposed sensing strategy. For more details, please refer to the SI.

FL imaging of living cells

All MDA-MB-231, Hela and LX2 cells were obtained from Hunan Fenghui Biotechnology Co., Ltd (Changsha, China). The cells were cultured in Dulbecco's Modified Eagle Medium (DMEM) and maintained in a humidified incubator at 37 °C with 5% CO_2. Subsequently, hydrogels prepared under different conditions were introduced into the cell culture medium. The mixture was incubated for 24 h in the CO_2 incubator. Subsequently, the cell culture medium was incubated for 1 h under both basal conditions (at 25 °C) and heat shock conditions (at 50 °C). Finally, the green FL of hydrogels was observed under an inverted FL microscope (Model IX73, Olympus, Tokyo, Japan). FL imaging was used to evaluate the influence of temperature and target on the fluorescence of the smart DNA hydrogel, and cells were introduced into different hydrogel states. To assess the effect of various target concentrations (0.1 fM, 1 pM and 10 nM) on the FL behavior of DNA-based hydrogels, target molecules at different concentrations were added to the cells. The FL variations were then observed using a total internal reflection FL microscope (TIRFM; Olympus IX73).

Conclusions

In this study, a spatially confined "double-key lock" smart DNA hydrogel integrating temperature responsiveness and nucleic acid recognition was successfully developed and combined with the RCA amplification strategy for dynamic FL detection of miRNA-21 secreted by cells. The synergistic response of the hydrogel to thermal stimulation and cDNA binding induced rapid crosslinking, forming a dense nanonetwork structure that restricted TCPE nanomaterial motion and maximized AIE-based fluorescence output. At high temperature (50 °C > LCST) thermal stimulation provided a "dynamic drive" by destroying the hydrogen bonds in the hydrogel and strengthening the hydrophobic interaction, while cDNA used the specific molecular recognition through base complementary pairing to act as "structure oriented". In this process, TCPE nanomaterials were highly aggregated due to the spatial limitation caused by the shrinking of hydrogel, while non-radiative transition movements such as rotation and vibration within TCPE nanomaterials were restricted, thus maximizing the activation of the AIE-FL effect. Thus, the developed DNA hydrogel showed excellent analytical performance for detection of miRNA-21 in the serum of cancer patients. The innovation of this work lies in the fact that stimulus responsive materials, aggregation induced emission, and nucleic acid amplification were combined to achieve dynamic detection of miRNA secreted by cells. This detection strategy possesses excellent biocompatibility, high nucleic acid recognition specificity, sensitive temperature response characteristics and *in situ* dynamic analysis capability, providing new technical support for the precise identification of abnormal tumor cell phenotypes. The strategy demonstrates the potential of integrating stimuli-responsive polymers, AIE fluorophores, and nucleic acid amplification into a unified sensing platform. Overall, this work provides a conceptual and methodological foundation for designing multi-responsive smart materials for biosensing, dynamic molecular imaging, and drug delivery, offering broad prospects for next-generation bioanalytical and biomedical applications.

Author contributions

All authors have given approval to the final version of the manuscript.

Conflicts of interest

The authors declare no conflict of interest.

Data availability

The data supporting this article have been included as part of the supplementary information (SI). Supplementary information: additional information about the experimental texts, figures and tables, including reagents and apparatus; experimental procedures; mechanism analysis of miRNA detection by smart DNA hydrogel; nuclear magnetic resonance spectra; fluorescence intensity analysis; HPLC analysis; DSC thermograms analysis; contact angles analysis; gel electrophoresis analysis; optimization of experimental conditions for RCA and smart DNA hydrogel, theoretical calculation analysis, stability analysis; cytotoxicity analysis; cells imaging analysis. See DOI: https://doi.org/10.1039/d6sc03610d.

Acknowledgements

The authors are grateful for financial support from the National Natural Science Foundation of China (grant no. 22276080, W2431017, 22574067 and 22504046), the Natural Science Foundation of Shandong Province (grant no. ZR2024QB252), the Natural Science Foundation of Jiangsu Province (grant no. BK20211340), the Natural Science Foundation of Zhenjiang City (grant no. SH2023103), and the Postgraduate Research & Practice Innovation Program of Jiangsu Province (SJCX25_2545).

Notes and references

1 C. J. Ni, D. Chen, Y. Yin, X. Wen, X. L. Chen, C. Yang, G. C. Chen, Z. Sun, J. H. Wen, Y. R. Jiao, C. Y. Wang, N. Wang, X. X. Kong, S. H. Deng, Y. Q. Shen, R. Xiao, X. M. Jin, J. Li, X. Q. Kong, Q. Zhao and T. Xie, Shape memory polymer with programmable recovery onset, *Nature*, 2023, **622**, 748–753.

2 W. L. Hou, W. Mao, J. Sun, Z. Q. Liu, W. Shen, H. K. Lee and S. Tang, Targeting hydrogel for intelligent recognition and spatiotemporal control in cell-based therapeutics, *Adv. Sci.*, 2024, **11**, 2404172.

3 N. Ramani, J. Hwang, A. J. Anderson, J. Delgado, L. Hernández-López, C. A. Figg, P. H. Winegar and C. A. Mirkin, Leveraging protein-ligand and DNA interactions to control hydrogel mechanics, *J. Am. Chem. Soc.*, 2025, **147**, 17293–17302.

4 C. Liu, Q. Zhu, J. Kuang, X. Zhou, Z. Ma, C. Huang, J. Song, W. Shen, H. K. Lee and S. Tang, DNA hydrogel-based fluorescence biosensor packed in a three-dimensional-printed microextractor for direct tracking of free antibiotic resistance genes in wastewater treatment plants, *ACS Sens.*, 2026, **11**, 4024–4032.

5 X. Zhang, Hydro-locking in hydrogel for extreme temperature tolerance, *Science*, 2025, **387**, 967–973.

6 M. M. Chen, Y. Wang, J. Y. Zhang, Y. Peng, S. Li, D. P. Han, S. Y. Ren, K. Qin, S. Li and Z. X. Gao, Stimuli-responsive DNA-based hydrogels for biosensing applications, *J. Nanobiotechnol.*, 2022, **20**, 40.

7 Z. G. Wang, R. P. Chen, S. P. Yang, S. Li and Z. X. Gao, Design and application of stimuli-responsive DNA hydrogels: A review, *Mater. Today Bio*, 2022, **16**, 100430.

8 Y. H. Wei, Y. Y. Feng, K. Z. Wang, Y. H. Wei, Q. Li, X. L. Zuo, B. Li, J. Li, L. H. Wang, C. H. Fan and Y. Zhu, Directing the encapsulation of single cells with DNA framework nucleator-based hydrogel growth, *Angew. Chem., Int. Ed.*, 2024, **136**, e202319907.

9 Y. X. Li, M. F. Xu, D. Y. Wang, Z. Q. Liu, W. Mao, J. Sun, W. Shen, H. K. Lee and S. Tang, Phase-changing NIPAM-AM/ATO hydrogels for thermochromic smart windows with highly adaptive solar modulation, *Chem. Eng. J.*, 2024, **499**, 156394.

10 K. Wang, X. Li, Y. Wei, Y. Feng, C. Mu, Z. Ge, Q. Li, Y. Zhu, J. Li, J. Wu and C. Fan, Dictating the fate of female germline stem cells using stiffness-programmed DNA hydrogels, *Cells Biomater.*, 2025, **1**, 100144.

11 Y. Zhou, M. Ye, C. Z. Hu, H. H. Qian, B. J. Nelson and X. P. Wang, Stimuli-responsive functional micro-/nanorobots: a review, *ACS Nano*, 2023, **17**, 15254–15276.

12 Y. Alsaid, S. W. Wu, D. Wu, Y. J. Du, L. X. Shi, R. Khodambashi, R. Rico, M. T. Hua, Y. C. Yan, Y. S. Zhao, D. Aukes and X. M. He, Tunable sponge-like hierarchically porous hydrogels with simultaneously enhanced diffusivity and mechanical properties, *Adv. Mater.*, 2021, **33**, 2008235.

13 Z. Y. Su, L. H. Xiong, J. Zhang, B. Z. Tang and X. W. He, Targeted recognition, fluorescent tracking and augmented killing of multi-bacterial infections *via* synergizing a magnetic bead-armored phage cocktail with enzyme-activated AIE probes, *Chem. Sci.*, 2025, **16**, 10813–10825.

14 X. Yan, T. H. Wang, H. X. Li, L. N. Zhang, H. Xin and G. Y. Lu, Flexible aggregation-induced emission-active hydrogel for on-site monitoring of pesticide degradation, *ACS Nano*, 2022, **16**, 18421–18429.

15 S. H. Jiang, F. Y. Liu, A. Lerch, L. Ionov and S. Agarwal, Unusual and superfast temperature-triggered actuators, *Adv. Mater.*, 2015, **27**, 4865–4870.

16 Y. P. Liang, J. H. He and B. L. Guo, Functional hydrogels as wound dressing to enhance wound healing, *ACS Nano*, 2021, **15**, 12687–12722.

17 X. Q. Xu, Y. Lyu, D. Liu, X. Y. Shi, Z. Y. Ji, D. S. Liu, X. Jia and X. L. Wang, Skin-mountable thermo-responsive structured hydrogel for optical and Adhesion coupled functional sensing, *Small*, 2025, **21**, 2411808.

18 N. B. Shustova, B. D. McCarthy and M. Dinca, Turn-on fluorescence in tetraphenylethylene-based metal-organic frameworks: an alternative to aggregation-induced emission, *J. Am. Chem. Soc.*, 2011, **133**, 20126–20129.

19 H. C. Shen, F. Y. Sun, X. Y. Zhu, J. Y. Zhang, X. W. Ou, J. Q. Zhang, C. H. Xu, H. H. Y. Sung, I. D. Williams, S. J. Chen, R. T. K. Kwok, J. W. Y. Lam, J. W. Sun, F. Zhang and B. Z. Tang, Rational design of NIR-II AIEgens with ultrahigh quantum yields for photo- and chemiluminescence imaging, *J. Am. Chem. Soc.*, 2022, **144**, 15391–15402.

20 D. W. Shi, D. H. Ji, X. Li, Z. C. Guan, M. H. Li and J. Bae, Firefly-inspired 3D printable multi-stimuli-responsive fluorescent hydrogels with adaptive luminescence, *ACS Nano*, 2025, **19**, 19578–19589.

21 Y. B. Hu, L. Barbier, Z. Li, X. F. Ji, H. Le Blay, D. Hourdet, N. Sanson, J. W. Y. Lam, A. Marcellan and B. Z. Tang, Hydrophilicity-hydrophobicity transformation, thermoresponsive morphomechanics, and crack multifurcation revealed by AIEgens in mechanically strong hydrogels, *Adv. Mater.*, 2021, **33**, 2101500.

22 F. Y. Yang, Y. F. Ou, J. L. Zhou, P. Z. Liang, T. B. Ren, X. B. Zhang and L. Yuan, Hydrogen-bond network-directed controllable assembly of stable cyanine j-aggregates for long-term and high-contrast in vivo imaging, *Angew. Chem., Int. Ed.*, 2026, **65**, e24960.

23 J. Zhang, H. Y. Xu, W. F. Fang, X. Liu, H. K. Zhang, R. K. Tang and Z. M. Liu, Calcium carbonate as an ionic molecular lock for ultrastrong fluorescence of single organic molecules, *Angew. Chem., Int. Ed.*, 2025, **137**, e202415664.

24 M. Qing, Y. J. Hou, Z. L. Xie, G. X. Qu, M. H. Chen and D. B. Guo, Thermal-triggered polymerizable hydrogels with localized hyperthermia for shrinkage-driven starvation therapy, *Adv. Funct. Mater.*, 2025, **36**, e12839.

25 J. P. Tang, Z. Cui, Q. Li, B. Ke, P. F. Liu, D. Y. Yang and C. Yao, DNA nanotechnology-engineered supramolecular hydrogel biosensor for cancer diagnosis via extracellular vesicles, *Adv. Funct. Mater.*, 2025, **36**, e12115.

26 G. Li, J. W. Chen, Z. A. Yan, S. C. Wang, Y. J. Ke, W. Luo, H. R. Ma, J. G. Guan and Y. Long, Physical crosslinked

hydrogel-derived smart windows: anti-freezing and fast thermal responsive performance, *Mater. Horiz.*, 2023, **10**, 2004–2012.

27 W. H. Chen, W. Mao, Z. Q. Liu, W. L. Hou, N. Kumar, J. Sun, X. W. Cai, C. Huang, W. Shen, F. Yang, Y. J. Cui, H. K. Lee and S. Tang, Photocatalytic degradation of bisphenol a by temperature-sensitive magnetic hydrogel with enhanced service life, *J. Hazard. Mater.*, 2023, **459**, 132188.

28 Y. Xiao, Y. Q. Bao, L. Liu, W. L. Xu, D. Li, X. Zheng, G. Z. Qin and Q. Li, A bio-inspired thermo-responsive hydrogel purifier for effective water harvesting in seawater, *J. Mater. Chem. A*, 2025, **13**, 30073–30083.

29 M. X. Li, R. J. Liu, T. Wang, L. Duo, G. Chen, M. F. Mao, Y. Sun, Y. Li, S. M. Cai, W. Q. Zhou, H. B. Lai and K. Ding, Human gut *Bifidobacterium longum* subsp. *suillum* is enriched in vitro by a pectic polysaccharide isolated from the flowers of *Lilium lancifolium*, *Carbohydr. Polym.*, 2025, **364**, 123772.

30 J. C. Dong, Y. Zhang, Z. Y. Yang, Y. H. Rao, Y. Y. Feng, L. Y. Huang, S. W. Xu, G. F. Wang and N. N. Liu, Highly sensitive detection of estradiol using glass micropipette constructed via polydopamine nanotubes filling and small molecule-induced DNA strand dissociation, *Anal. Chem.*, 2025, **97**, 22418–22426.

31 Y. T. Ji, Y. Yuan, F. M. Peng, S. Y. Fu, B. Liu, Z. Y. Dong, Q. Li, S. C. Ma and Z. M. Ao, Two-component hydrogels built from chinese herbal medicine-derived glycyrrhizic acid and puerarin: assembly mechanism, self-healing properties, and selective antibacterial activity, *ACS Appl. Mater. Interfaces*, 2025, **17**, 5223–5231.

32 P. K. Marvi, P. Das, A. Jafari, S. Hassan, H. Savoji, S. Srinivasan and A. R. Rajabzadeh, Multifunctional carbon dots in situ confined hydrogel for optical communication, drug delivery, pH sensing, nanozymatic activity, and UV shielding applications, *Adv. Healthc. Mater.*, 2025, **14**, 2403876.

33 S. J. Wang, J. Wang, L. F. Zhu, C. X. Li, J. X. Wu, S. G. Ge and J. H. Yu, Aptamer responsive DNA functionalized hydrogels electrochemiluminescence biosensor for the detection of adenosine triphosphate, *Biosens. Bioelectron.*, 2024, **261**, 116476.

34 C. T. Wen, Z. Y. Zhang, G. Y. Liu, Y. D. Li, L. Liang, X. F. Liu, X. Xu and J. X. Zhang, Structure, rheology and gastrointestinal release kinetics of new-type curcumin-based nanofibers nanohydrogel assisted prepared with subcritical water at different treatment times, *Food Hydrocoll.*, 2023, **145**, 109156.

35 C. Liu, C. W. He, X. B. Dai, L. Yan and H. P. Xu, Achieving mechanical evolution in polymer materials through phase evolution induced by visible light, *Adv. Mater.*, 2025, **37**, e08549.

36 B. Mahaling, C. Roy and S. Ghosh, Silk-gelatin hybrid hydrogel: a potential carrier for RNA therapeutics, *J. Mater. Chem. B*, 2024, **12**, 6203–6220.

37 Y. X. Hu, J. H. Zhang, K. Shen, W. Shen, H. K. Lee and S. Tang, Intelligent molecular logic computing toolkits: nucleic acid-based construction, functionality, and enhanced biosensing applications, *Chem. Sci.*, 2025, **16**, 20139–20180.

38 X. Dong, J. Liang, A. F. Yang, Z. Y. Qian, D. L. Kong and F. Lv, Fluorescence imaging guided CpG nanoparticles-loaded IR820-hydrogel for synergistic photothermal immunotherapy, *Biomaterials*, 2019, **209**, 111–125.

39 X. X. Du, Y. H. Bi, P. P. He, C. Y. Wang and W. W. Guo, Hierarchically structured DNA-based hydrogels exhibiting enhanced enzyme-responsive and mechanical properties, *Adv. Funct. Mater.*, 2020, **30**, 2006305.

40 D. Ji, L. Tang and J. Bae, Muscle-mimetic thermomechanical adaptive hydrogels capable of isometric exercise, *Adv. Funct. Mater.*, 2025, **36**, e19482.

41 S. Plimpton, Fast parallel algorithms for short-range molecular dynamics, *J. Comput. Phys.*, 1995, **117**, 1–19.

42 A. Stukowski, Visualization and analysis of atomistic simulation data with OVITO-the open visualization tool, *Model. Simul. Mater. Sci.*, 2010, **18**, 015012.

43 J. J. Winetrout, K. Kanhaiya, J. Kemppainen, P. J. in 't Veld, G. Sachdeva, R. Pandey, B. Damirchi, A. van Duin, G. M. Odegard and H. Heinz, Implementing reactivity in molecular dynamics simulations with harmonic force fields, *Nat. Commun.*, 2024, **15**, 7945.

44 G. Bussi, D. Donadio and M. Parrinello, Canonical sampling through velocity rescaling, *J. Chem. Phys.*, 2007, **126**, 014101.

45 S. B. Yu, G. L. Wei, P. Zhao, J. Zhang, J. M. Kong and X. J. Zhang, Organic small molecule catalytic PET-RAFT electrochemical signal amplification strategy for miRNA-21 detection, *Chem. Eng. J.*, 2024, **492**, 152380.

46 Y. X. Zhu, Z. H. Liang, P. L. Wang, Q. Ma and Z. Q. Zhang, An electrochemiluminescence sensor with wide stable potential detection window based on superhydrophilic amino acid polyionic liquid for the detection of miRNA-128 in colorectal cancer, *Biosens. Bioelectron.*, 2025, **282**, 117502.

47 Q. H. Jiang, J. Zhou, Y. W. Sha, M. S. Jiang, Y. Q. Chai and R. Yuan, A multifunctional tetrahedral DNA nanostructure for the simultaneous sensitive detection and imaging of miRNA and zinc ions in living cells, *Anal. Chem.*, 2025, **97**, 13368–13375.

48 M. A. Yin, J. Jiao, L. N. Lu, B. X. Hu, L. Xue, F. J. Dai, X. R. Wang, Z. J. Wang, T. Wang and Q. Chen, A simultaneous strategy with multiple-signal amplification and self-calibration for ultrasensitive assay of miRNA-21 based on 3D MNPs-IL-rGO-AuNPs, *Biosens. Bioelectron.*, 2024, **249**, 116009.

49 J. L. Teng, Y. P. Chen, W. W. Zhang, H. T. Xu, L. F. Ke, H. Xu and J. Wang, An RCA-CRISPR-Enhanced SERS platform for ultrasensitive and single-nucleotide-resolved detection of exosomal miRNA-21 in early lung cancer, *Anal. Chem.*, 2025, **97**, 21098–21105.

50 S. B. Seo, J. Lim, K. Kim, I. Maeng, H. W. Rho, H. Y. Son, E. Kim, E. Jang, T. Kang, J. Jung, S. J. Oh, Y. M. Huh and E. K. Lim, Nucleic Acid Amplification Circuit-Based Hydrogel (NACH) assay for one-step detection of metastatic gastric cancer-derived exosomal miRNA, *Adv. Sci.*, 2024, **11**, 2407621.

51 X. Zhu, L. L. Liu, W. W. Cao, R. Yuan and H. J. Wang, Ultrasensitive microRNA biosensor based on strong aggregation-induced electrochemiluminescence from bidentate ligand-stabilized copper nanoclusters in polymer hydrogel, *Anal. Chem.*, 2023, **95**, 5553–5560.

52 C. H. Yu, X. Yang, B. Yang, W. Y. Li, J. B. Wang and H. J. Liu, Dual amplification DNA reactions for ultrasensitive electrochemical biomolecular detection using impedimetric biosensor, *Biosens. Bioelectron.*, 2025, **287**, 117707.

53 Y. F. Wang, Y. Y. Fang, Y. Zhu, S. Y. Bi, Y. Liu and H. X. Ju, Single cell multi-miRNAs quantification with hydrogel microbeads for liver cancer cell subtypes discrimination, *Chem. Sci.*, 2022, **13**, 2062–2070.

54 K. Li, X. Yu, Y. T. Xu, H. X. Wang, Z. Liu, C. Wu, X. Luo, J. C. Xu, Y. Q. Fang, E. G. Ju, S. X. Lv, H. F. Chan, Y. H. Lao, W. L. He, Y. Tao and M. Q. Li, Cascaded immunotherapy with implantable dual-drug depots sequentially releasing STING agonists and apoptosis inducers, *Nat. Commun.*, 2025, **16**, 1629.

55 J. W. Wu, X. M. Zeng, L. A. Wang, J. H. Zhang, S. H. Cui, Z. X. Ma, R. R. Pan, C. Liu, D. Z. Kong, J. Song, L. Liu, C. Y. Feng, W. Shen, X. C. Suo, Z. X. Lin, H. K. Lee and S. Tang, Embedding carbon nanotubes in artificial cells enhances probe transfer, *Adv. Mater.*, 2025, **37**, 2418271.

56 H. Yan, Y. J. Wen, Z. M. Tian, N. Hart, S. Han, S. J. Hughes and Y. Zeng, A one-pot isothermal Cas12-based assay for the sensitive detection of microRNAs, *Nat. Biomed. Eng.*, 2023, **7**, 1583–1601.

57 Z. Y. Ma, J. J. Xu, W. L. Hou, Z. Lei, T. T. Li, W. Shen, H. Yu, C. Liu, J. H. Zhang and S. Tang, Detection of single nucleotide polymorphisms of circulating tumor DNA by strand displacement amplification coupled with liquid chromatography, *Anal. Chem.*, 2024, **96**, 5195–5204.